

Machine learning-based multipoint optimisation for improving aerodynamics of symmetrically cambered wing sails in wind-assisted ship

Downloaded from: https://research.chalmers.se, 2025-11-07 03:23 UTC

Citation for the original published paper (version of record):

van Reen, S., Serbülent, B., Yao, H. (2025). Machine learning-based multipoint optimisation for improving aerodynamics of symmetrically cambered wing sails in wind-assisted ship propulsion. Ocean Engineering, 342(1). http://dx.doi.org/10.1016/j.oceaneng.2025.122829

N.B. When citing this work, cite the original published paper.

research.chalmers.se offers the possibility of retrieving research publications produced at Chalmers University of Technology. It covers all kind of research output: articles, dissertations, conference papers, reports etc. since 2004. research.chalmers.se is administrated and maintained by Chalmers Library

ELSEVIER

Contents lists available at ScienceDirect

Ocean Engineering

journal homepage: www.elsevier.com/locate/oceaneng



Research paper

Machine learning-based multipoint optimisation for improving aerodynamics of symmetrically cambered wing sails in wind-assisted ship propulsion

Stephan van Reen*, Berken Serbülent, Hua-Dong Yao 🗓

Chalmers University of Technology, Department of Mechanics and Maritime Sciences, Sweden

ARTICLE INFO

Keywords: Machine learning Neural networks Aerodynamics Multipoint optimisation Rigid wing sail Wind-assisted ship propulsion

ABSTRACT

The threat of climate change has renewed interest in sailing as a carbon-neutral propulsion method, with rigid wing sails emerging as promising auxiliary systems. A new class of wing sails that is symmetric about the half chord (also termed crescent-shape in the literature) has enabled the introduction of camber to enhance thrust production. They are particularly suited for wind-assisted ship propulsion, where performance across a wide range of apparent wind angles is critical. However, their aerodynamic shape remains largely unoptimised. To address this, an efficient aerodynamic optimisation method was developed by integrating a neural network-based aerofoil simulation tool and a Bayesian optimisation framework. The optimisation strategy guided the search for maximum average thrust across apparent wind angles from 10° to 150°, using a Gaussian Process surrogate model to balance exploration and exploitation. Aerofoil profiles were sampled through hybrid geometry parametrisation that combines Bézier curve-specified camber and modified NACA 4-digit thickness distribution. Sensitivity analysis revealed that larger tip radii and reduced maximum thickness can improve thrust production. The optimised geometry, termed BN4, was adopted to construct a full-size wing sail configuration. This configuration together with a benchmark configuration were simulated using the Improved Delayed Detached Eddy Simulation (IDDES). The simulation results indicated that the optimisation alleviates flow separation and increases pressure magnitudes on the suction side of the profile. This work demonstrates a path for the use of machine learning techniques in aerodynamic optimisation for wing sails, and sheds light on geometric parameters dominating the specific thrust production.

1. Introduction

Sailing was the primary form of transportation across water until combustion engines were widely equipped in the 19th century (Khan et al., 2021). However, with the increasing threat of climate change, the modern shipping industry endeavours to reincorporate wind power as auxiliary or main propulsion (Zhu et al., 2023b).

The auxiliary propulsion is collectively referred to as Wind-Assisted Ship Propulsion (WASP), and it encompasses various technologies. Notable examples include Flettner rotors, kite rig propulsion, traditional soft sails, and rigid wing sails.

Soft sails provide an easily adjustable solution for varying wind conditions, offering quick storage, simple repairs, and reliable performance in diverse operational scenarios (Neal et al., 2009). However, they require constant adjustment to maintain their shape, particularly near headwinds, which increases operational complexity and cost. Additionally, their extensive rigging can interfere with deck activities such as

cargo handling. Rigid sails address many limitations of soft sails Silva et al. (2019). Their nearly constant aerodynamic shape enables more efficient operation near headwind conditions. The structural stiffness can reduce wear and tear, and the higher lift-to-drag ratio can lead to smaller heeling moments.

The introduction of rigid wing sails in the 2010 America's Cup marked a turning point in sail technology development due to their superior performance (Blakeley et al., 2012). Such a rigid sail consists of two foils, resembling an aircraft wing with a high-lift device. Blakeley et al. (2012) performed wind tunnel tests for a two-element wing sail. They showed that the size of the gap between the two foil elements significantly affects the angle of stall. Later Furukawa et al. (2015) found that compared to the gap size and pivot point, flap deflection plays a dominant role in the lift and drag generation. They also observed that at high camber and angle of attack (AOA), Reynolds numbers below 6×10^5 lead to early flow separation and poor aerodynamic performance. Li et al.

E-mail addresses: stephan.vanreen@chalmers.se (S. van Reen), berken@chalmers.se (B. Serbülent), huadong@chalmers.se (H.-D. Yao).

^{*} Corresponding author.

Ocean Engineering 342 (2025) 122829

(2020) expanded the analysis using two- and three-dimensional (2D and 3D) CFD simulations. They showed that at large flap deflections, stall can be delayed by moving the flap rotation axis aft and increasing the flap thickness. Especially the lift increases when the flap rotation axis is placed between 85-95 % of the chord. Recent research by Hillenbrand et al. (2024) investigated stall behaviour through wind tunnel experiments. A two-stage stall was revealed, and it involves an initial flap stall followed by full wing separation that exhibits hysteresis effects. Additionally, a wing sail design investigated by Jo et al. (2013) incorporates a morphing wing equipped with a hinged flap. By deflecting the flap, the lift is increased. This design is similar to the two-element one, while its flap is merged into the wing so that no gap is formed to affect the aerodynamic performance.

Alternatively, symmetrically cambered (also termed crescentshaped) wing sails have attracted growing interest. These are singleelement aerofoils that generate high thrust across a wide range of angles of attack (van Reen et al., 2025). Their simple structure also allows for telescopic size adjustment to suit weather conditions (Zhu et al., 2023b). Ouchi et al. (2011) introduced the concept of a "motor-assisted sailing ship" equipped with nine telescopically adjustable symmetrically cambered wing sails, projecting up to 50% energy savings when sailing with the Trade Winds. This concept evolved into the "Wind Challenger" (Ouchi et al., 2016), featuring four wing sails and estimated to reduce energy use by around 30% on a voyage between Yokohama and Seattle. In 2022, the bulk carrier Shofu Maru was fitted with a single Wind Challenger sail, installed on the forecastle (Ouchi et al., 2023). Fuel savings were estimated at 5% on routes between Japan and Eastern Australia, and 8% on routes to the west coast of North America (Ouchi et al., 2023).

Expanding on the practical implementation of symmetrically cambered wing sails, research into their aerodynamic performance has advanced significantly. Zhu et al. (2022) proposed a refinement to the basic crescent shape. They conducted a parametric study using the Computational Fluid Dynamics (CFD) method, the unsteady Reynolds-Averaged Navier-Stokes (RANS) equations, to evaluate various geometric configurations. A geometry termed "D2R10" was identified with the best lift generation. Building on this, Zhu et al. (2023b) carried out a detailed numerical analysis of D2R10 using unsteady RANS, and it was further refined by Zhu et al. (2024) through Improved Delayed Detached Eddy Simulation (IDDES) to capture more complex flow behaviour. Additionally, Zhu et al. (2023a) conducted wind tunnel tests on three inline D2R10 wing sails under varying wind speeds, apparent wind angles (AWAs), and AOAs. They found that the front sail generated the most thrust, the aft the least, and the middle sail experienced the highest structural vibrations.

To achieve efficient aerodynamic performance, sectional profiles of wing sails were optimised by scholars. Makram et al. (2023) optimised a flapped morphing wing sail configuration for a Suezmax tanker using the Taguchi method aided with RANS. There were 13 symmetrical profiles evaluated in the 2D XFOIL code (Drela, 1989), and one was selected for its high lift, low drag, low pitching moment, and smooth stall behaviour at moderate-to-high Reynolds numbers. This profile was applied to construct 9 configurations, varying in aspect ratio, taper ratio, and number of wing sail pairs. The study also showed that neglecting aerodynamic interferences between sails could significantly overestimate performance. Guzelbulut et al. (2024) optimised the D2R10 profile by varying three design parameters at three levels to enhance the thrust or reduce the propeller power. Using the Taguchi method, 9 out of 27 combinations were selected for CFD simulations across a range of AOAs and wind directions. The best-performing angles were averaged for each design, and the results were used to train a second-order polynomial surrogate model. The thrust-optimised design increased the thrust by 12.3%, while the power-optimised design reduced the required power by 22 % compared to the original.

Aside from sectional profile optimisation, the optimisation of multiple-sail installation layout was investigated to minimise aerody-

namic interference effects between installed sails. Jo et al. (2013) investigated the optimal operating conditions for three morphing-wing sails arranged in a line. Using a Kriging surrogate model combined with a genetic algorithm, they optimised nine design parameters, including deflection angle, flap length and angle of attack. Their results predicted a 10% increase in thrust. Hussain and Amin (2021) used steady RANS to estimate the thrust generated by a bulk carrier equipped with five rigid wing sails. NACA 4412 was adopted as the sail profile, which is adaptive to winds from one board side. The simulations predicted a reduction in required brake power by 30% at zero drift and 20% at higher drift angles. Yasuda et al. (2024) numerically simulated interactions between two symmetrically cambered rigid sails. Their work aimed to optimise AOAs for maximum thrust at AWAs of 150° and 180°. They found that a low fore and high aft angle of attack is optimal at 150°, while the reverse is more effective at 180°, emphasising the role of sail configuration and control in enhancing propulsion efficiency. Malmek et al. (2024) extended the lifting line model developed by Malmek (2023) to simulate multiple wing sails. This enhanced model incorporates a potential flow-based interaction method and an optional boundary layer correction, enabling more accurate prediction of 3D aerodynamic forces in upwind conditions while maintaining computational efficiency. van Reen et al. (2025) evaluated triple in-line and quad parallel layouts for symmetrically cambered sails, using a hybrid method that combines a genetic algorithm and a Kriging surrogate model to optimise sail spacing under a fixed total distance. The in-line layout showed only 4% to 6% thrust loss due to aerodynamic interference, compared to up to 28% in the parallel layout. Although optimisation yielded slight gains, relaxing spacing constraints appeared more effective.

As the research into wing sail design matures and computing power increases, machine learning optimisation of wing sails has become a viable way to improve wing sail designs. Ma et al. (2019) proposed a coupled wing sail design that combines an arc-shaped wing with a NACA0018 aerofoil to improve aerodynamic performance. They used the modified PARSEC method to define 14 geometric parameters and applied the Particle Swarm Optimisation (PSO) to maximise the power factor, defined as $C_L^{1.5}/C_D$, across AOAs from -15° to 40°. And an optimal AOA was selected for each wind speed. The final metric, a weighted sum of power factors, showed a 30% improvement over the original arc-shaped sail in the optimal configuration. A notable aspect of Ma et al. (2019) is the maximization of the power factor, which implicitly penalizes drag and favours aerodynamic efficiency. This approach aligns with conventional aircraft optimisation strategies (Huang et al., 2020a,b), which prioritize low drag and stall avoidance by operating at low AOAs

However, such strategies are not directly applicable to wing sail design. Unlike aircraft wings that aim to generate lift, wing sails produce thrust from lift, drag, or both, depending on the AWA (Zhu et al., 2023b; Hillenbrand et al., 2024). Consequently, they must perform across a broader range of AOAs, including deep-stall conditions. Wing sails are often operated under tailwinds or high-AOA scenarios to maximize thrust, making their optimisation more complex. Instead of avoiding stall, the optimisation goal for wing sails should be to sustain high thrust under variable and unsteady wind conditions.

This study aims to optimise the aerodynamic performance of symmetrically cambered geometries for rigid wing sails. To address the unique challenges of wing sail design, this paper will propose an optimisation framework tailored to their complex performance requirements. Given the wide range of apparent wind angles (AWAs) and the need for extensive parametric sampling, machine learning techniques will be incorporated to reduce computational costs. Aerofoil profiles will parametrised using a hybrid camber and thickness definition featuring six adjustable parameters. The sensitivity of the flow field to the parameters will be addressed. The optimised geometry and a benchmark geometry from a previous work (Zhu et al., 2023b) will then be assessed through the high-fidelity CFD method of the Improved Delayed

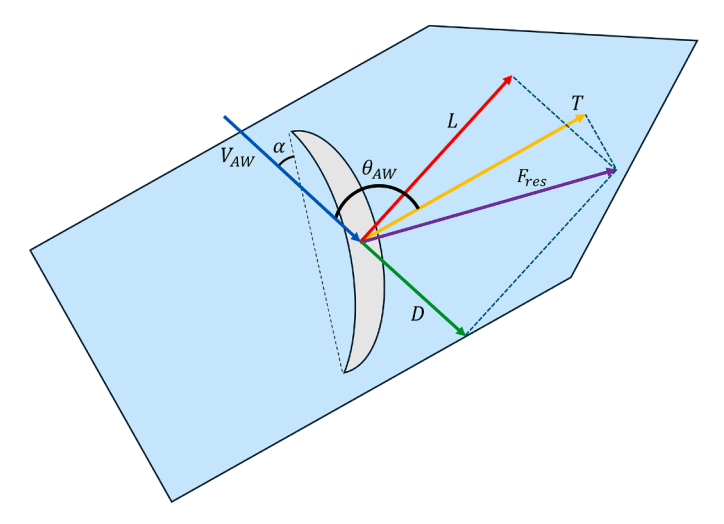


Fig. 1. Diagram of the AOA (α), lift (L), drag (D), resultant aerodynamic force (F_{res}) and thrust (T) with respect to the apparent wind vector (V_{AW}) at the AWA (θ_{AW}).

Detached Eddy Simulation (IDDES), to explore dominant aerodynamic mechanisms.

This paper is organized by starting with an overview of the optimisation method and the setup of the high-fidelity simulations. The result section presents and discusses the method validation and the aerodynamic performance of the optimised design in reference to the benchmark configuration. Lastly, the conclusions are drawn, and the future work is pointed out.

2. Method

2.1. Objective selection

The primary purpose of a sail is to provide thrust, which naturally makes it the most important optimisation objective to maximise. The thrust vector can be defined as the component of the resultant aerodynamic force F_{res} in the movement direction of the ship. This definition is shown in Fig. 1, where the AOA is α , V_{AW} is the apparent wind vector, L is the lift, D is the drag, and T is the thrust. From this definition, an equation for the thrust can be derived:

$$T = L(\alpha) \cdot \sin(\theta_{AW}) - D(\alpha) \cdot \cos(\theta_{AW}) , \qquad (1)$$

where θ_{AW} denotes the AWA, and L and D are dependent on α . When non-dimensionalised, the thrust, lift and drag coefficients are defined as:

$$C_l = \frac{T}{\frac{1}{2}\rho V_{\infty}^2 c}, \qquad C_l = \frac{L}{\frac{1}{2}\rho V_{\infty}^2 c}, \qquad C_d = \frac{D}{\frac{1}{2}\rho V_{\infty}^2 c},$$
 (2)

where ρ is the air density, V_{∞} is the speed of the incoming flow and c is the chord of the aerofoil.

The wind angle observed by an external observer is called the true wind angle (TWA). When the ship is stationary, the AWA and TWA are identical. Only the apparent wind needs to be considered for the purpose of aerodynamics, as this determines the wind force applied to sails (Kimball, 2009). The AWA is counted as counter-clockwise when looking at the ship from above, as shown in Fig. 2.

According to Eq. 1, the thrust coefficient varies directly with the AWA and indirectly with the AOA through C_l and C_d . A wing sail can fully rotate in the horizontal plane, that is, be freely adjustable to any AOA. Thus, for an arbitrary AWA, the thrust is calculated for the AOA that provides the highest thrust. This thrust variance means that one cannot simply assign a single thrust value to a certain geometry. Instead, the optimisation objective is not strictly the thrust but the average thrust

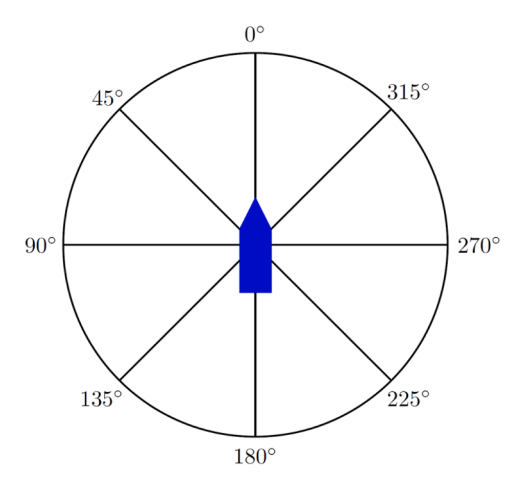


Fig. 2. Definition of the apparent wind angle θ_{AW} from a top-down view, where the ship is in blue.

over a range of AWAs. This yields:

$$\overline{C}_t = \frac{1}{N} \sum_{i=1}^{N} C_{t,i} , \qquad (3)$$

where 'i' represents the ith AWA of interest, and 'N' is the total number of angels.

2.2. Geometric parametrisation

In this study, a new hybrid parametrisation method for symmetrically cambered aerofoils proposed by Yao (2025) will be used to generate various geometric samples during the optimisation process. The parametrisation is formulated in reference to NACA-series foils and cambers.

The reference camber height distribution is based on the camber line definition of a NACA 4-digit aerofoil (Jacobs et al., 1933). For the camber section upstream of the position of the maximum camber height, the camber height y_c is defined as:

$$\frac{y_c}{c} = \frac{h_c}{c} \left[2\frac{x}{x_c} - \left(\frac{x}{x_c}\right)^2 \right] \quad 0 \le x \le x_c \tag{4}$$

where h_c is the maximum camber height, x_c the location of h_c , and c the chord length. Since the camber of the crescent aerofoil is symmetric, we choose this upstream camber section to construct the crescent camber by setting $x_c/c=0.5$ and mirroring the upstream section to form the downstream one. This gives:

$$\frac{y_c}{c} = \frac{4h_c}{c} \left[\frac{x}{c} - \left(\frac{x}{c} \right)^2 \right] \quad 0 \le \frac{x}{c} \le 1.$$
 (5)

Note that this definition only requires h_c as an input. The camber parametrisation is constructed using a Bézier curve defined by four control points. These points shape the curvature of the front half of the camber line, while the rear half is generated by mirroring the front. Control Point 1 (CP1) is fixed at the leading edge of the foil with nondimensionalised coordinates (x,y)=(0,0), and Control Point 4 (CP4) is fixed at $(x,y)=(0.5,h_c)$. In contrast, Control Points 2 and 3 are left unfixed to allow flexibility in adjusting the curvature. The initial Bézier curve is obtained by fitting it to the reference camber line defined in Eq. 5. The fitting process employs the *minimize* function from the Python library Scipy (Virtanen et al., 2020). It finds the CP2 and CP3 coordinates that minimise the least-squares error between the reference camber line and the Bézier curve.

Next, the thickness distribution of the aerofoil is parametrised based on the modified NACA 4-digit series (Mason, 2018). The front half of

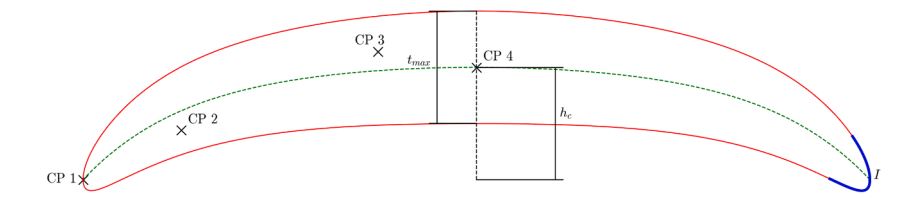


Fig. 3. A parameterized crescent airfoil with a camber that is symmetric about the middle point of the chord. The control points such as CP1–CP4 are used to define a Bézier curve for half of the camber line.

the thickness distribution is defined as:

$$\frac{y_t}{c} = 5\left(\frac{h_t}{c}\right) \left[a_0\sqrt{\frac{x}{c}} + a_1\left(\frac{x}{c}\right) + a_2\left(\frac{x}{c}\right)^2 + a_3\left(\frac{x}{c}\right)^3\right] \quad 0 \le \frac{x}{c} \le 0.5 \quad (6)$$

where h_t is the maximum thickness. The coefficient a_0 reads:

$$a_0 \approx 0.296904 \cdot \chi_{LE} \tag{7}$$

and

$$\chi_{LE} = \begin{cases} I/6 & \text{for } I \le 8\\ 10.3933 & \text{for } I = 9 \end{cases}$$
 (8)

where I is the index used to specify the leading edge radius. The other coefficients are:

$$a_1 \approx 0.477 - 2.650a_0 \tag{9}$$

$$a_2 \approx -0.708 + 3.536a_0 \tag{10}$$

$$a_3 \approx 0.308 - 2.121a_0 \tag{11}$$

According to Eqs. (6)–(11), the definition of the thickness distribution needs h_t and I as inputs. Using the same method as for constructing the whole camber line, the front half of the thickness distribution is mirrored about x/c = 0.5, to create a symmetric thickness distribution.

The new camber line and thickness distribution are then combined to create a symmetrically cambered aerofoil. A geometry example and its parameters are illustrated in Fig. 3. The adjustable parameters are the leading edge radius index I, the maximum thickness h_t , and the x and y-coordinates of the control points, CP2 and CP3, of the Bézier curve.

2.3. Parameter constraints

The variation ranges of the geometric parameters for the proposed crescent foil are constrained with reference to the D2R10 foil studied by Zhu et al. (2023b), as its structural viability has been validated by the industry in prior studies. By doing this, the superior performance of the optimal geometry can be identified in comparison to D2R10.

The minimum thickness of the D2R10 was required to provide space for the mast, and it corresponds to $14.29\%\,c$. This value serves as the lower bound of the foil thickness h_t , as well as its reference. The upper bound is set to 20% above the reference. The maximum camber height, h_c , is fixed at the same value as that of the D2R10 reference aerofoil, specifically $14.25\%\,c$ (Zhu et al., 2023b). This decision is motivated by preliminary studies indicating that h_c has a significant influence on the resulting aerodynamic forces. Since the primary goal of this study is to evaluate the effectiveness of the optimisation framework relative to the D2R10, it makes sense to maintain certain geometric features unchanged. Therefore, h_c is held constant to focus on the effects of other design variables and ensure a fair comparison with the reference configuration.

The control point coordinate bounds can vary 5 % from the reference coordinates, which are obtained by fitting the Bézier curve to the reference NACA 4-digit camber line. The radius index of the leading and trailing edges (LE and TE) is bounded between 4 and 8. The constraints for each feature are summarised in Table 1.

In addition to the parameter constraints described above, curvature constraints are further set to filter abnormal geometries that consist of wavy curve segments (Yao et al., 2022). In these constraints, the slope

 Table 1

 The constraints of the geometrical parameters for the crescent foil.

Variable	Feature	Lower bound	Reference	Upper bound	
LE/TE radius index	I	4	-	8	
Foil thickness (% c)	h_t	14.29	14.29	17.15	
CP2, x-position (% c)	x_2	17	22	27	
CP2, y-position (% c)	y_2	3	8	13	
CP3, x-position (% c)	x_3	33	38	43	
CP3, y-position (% c)	y_3	8	13	18	

of the front half of the camber line is always positive, and the second derivative along the front half changes sign no more than once. If a sample does not comply with the constraints, it is discarded and a new sample is generated until a suitable one is found.

2.4. Optimisation method

The Bayesian optimisation method is employed in this study (Snoek et al., 2012; Hebbal et al., 2021), where an objective function is minimised by approximating it with a probabilistic surrogate model, which in this case is a Gaussian Process (GP) (Snoek et al., 2012)

A GP is defined as a collection of random variables, where any finite subset of these variables has a joint Gaussian distribution (Rasmussen, 2004; Hebbal et al., 2021). It is specified by a prior mean function $m(\phi)$ and a prior covariance function $k(\phi, \phi')$, also known as a kernel, where ϕ and ϕ' are inputs in the input space Φ :

$$f(x) = GP(m(\phi), k(\phi, \phi'))$$
(12)

The mean function describes the prior belief about the trend of the function that the surrogate model seeks to approximate. If nothing is known, a constant mean function may be used. The covariance function captures the prior belief about the correlation between individual samples (Shan et al., 2025; Hebbal et al., 2021).

This study uses the Matérn kernel (Rasmussen and Williams, 2006), which is particularly suitable for modelling functions that are not overly smooth. The Matérn kernel with smoothness parameter v = 5/2 and a length scale l = 1 is defined as (Rasmussen and Williams, 2006):

$$k(\phi, \phi') = (1 + \sqrt{5} |\phi - \phi'| + \frac{\sqrt{5} (\phi - \phi')^2}{3}) \exp(-\sqrt{5} |\phi - \phi'|)$$
 (13)

The algorithm that creates a GP is called the Gaussian Process Regression (Rogers et al., 2023). When the GP observes sample data $S_o(\phi_o, \psi_o)$, with observed inputs ϕ_o and observed objective values ψ_o , it updates its prior beliefs to form a posterior distribution. This posterior is defined by a predictive mean $\mu_*(\phi_*)$ and variance $\sigma_*^2(\phi_*)$ (Rasmussen, 2004). These functions describe a Gaussian distribution over the objective value at any new input $\phi_* \in \Phi$, capturing both prediction and uncertainty (Snoek et al., 2012; Hebbal et al., 2021). The functions are defined as:

$$\mu_*(\phi_*) = k_*^T (K + \sigma_n^2 I)^{-1} \psi_o$$
 (14)

$$\sigma_{*}^{2}(\phi_{*}) = k(\phi_{*}, \phi_{*}) - k_{*}^{T} (K + \sigma_{*}^{2} I)^{-1} k_{*}$$
(15)

To guide the optimisation, an acquisition function is derived from the GP posterior. This function determines where to sample next by balancing exploration (uncertainty) and exploitation (high predicted value) S. van Reen et al. Ocean Engineering 342 (2025) 122829

(Wang et al., 2023). The acquisition function used in this study is the Upper Confidence Bound (UCB) defined as:

$$UCB(\boldsymbol{\phi}_*) = (\mu_*(\boldsymbol{\phi}_*) + k\sigma_*(\boldsymbol{\phi}_*)), \tag{16}$$

The parameter k controls the trade-off between exploration and exploitation (Snoek et al., 2012). A higher value of k encourages exploration by favouring regions with high uncertainty, while a lower value promotes exploitation of regions with high predicted objective values. In this study, k is set to 2.576, corresponding to the 99% confidence interval of a standard normal distribution.

The Bayesian optimisation algorithm was selected because of the complex nature of the relation between thrust and wing sail design. There is no closed-form expression to analyse, nor any gradient data, which makes gradient-based algorithms unusable. Instead, the optimiser must effectively explore the design space and balance this with exploitation (Wang et al., 2023). There are other algorithms that can do this, such a genetic algorithms and particle swarm optimisation, but these generally require more evaluations from the aerodynamic solver than Bayesian optimisation to find an optimum (Wang et al., 2023). Given that the current goal is the develop an optimisation framework that can be generalised to multiple aerodynamic solvers, including high-fidelity CFD, it is essential to decrease the required number of function evaluations.

The power of the Bayesian optimisation in this paper can largely be attributed to the GP surrogate model. The GP is a powerful algorithm that is incorporated in multiple other optimisation methods, such as dimensionality reduction with the GP Latent Variable Model (Li and Chen, 2016), GP for classification (Nickisch and Rasmussen, 2008) or reinforcement learning with the Probalilistic Inference Learning Control algorithm (Deisenroth and Rasmussen, 2011). But these are not suitable for the use as a surrogate model for a complicated aerodynamic function that predicts the thrust. By contrast, the Bayesian optimisation algorithm is able to harness the prediction capability and uncertainty estimation of the GP surrogate model to efficiently recreate black-box functions.

2.5. Training data acquisition

A hybrid sampling strategy is employed to generate the initial set of 100 samples used for training the surrogate model. The process starts with Sobol sampling, which provides uniform coverage of the input space. Each sample, composed of 6 feature values and the objective value \overline{C}_t , is then subjected to constraint checks related to the camber line. Samples that do not satisfy these constraints are discarded and replaced with new ones, ensuring that only valid configurations are retained. These validated samples form the basis for the initial surrogate model, which is further refined throughout the optimisation process.

The lift and drag coefficients used to calculate the thrust coefficient are computed using NeuralFoil (Sharpe, 2023), an aerofoil analysis software written in Python that utilises a physics-informed neural network for its predictions. NeuralFoil was trained based on results from XFOIL and is suitable for two-dimensional viscous, steady, incompressible and compressible aerodynamic analysis.

The predictions made by NeuralFoil are similarly accurate to XFOIL, but NeuralFoil is significantly faster (Sharpe and Hansman, 2025). Furthermore, convergence failure sometimes happens in XFOIL when it attempts complicated simulation tasks (Sharpe and Hansman, 2025). As a result, XFOIL cannot provide the necessary training data for the wide variety of aerofoil geometries that are required in this study. By contrast, NeuralFoil provides an answer for a large range of geometries it is given to analyse. NeuralFoil also incorporates analytical relations developed by Truong (2020) in its framework. These relations include C_l and C_d predictions over a 360° AOA range and models for moderate to deep stall. This shows that NeuralFoil not only utilizes XFOIL data but also builds upon it with enhanced predictive capabilities.

Wing sails ideally operate at the AOA that provides the maximum thrust, which is often found near the AOA of the maximum lift α_{max} (Malmek et al., 2024). Previous 3D simulations by Zhu et al. (2023b) showed that α_{max} for the D2R10 is 20°. While a wing sail ideally operates at the stall angle of attack, a sudden gust of wind can push the sail into stall conditions. Moreover, the aerofoils to be analysed in the optimisation are expected to have different stall characteristics than the D2R10. Therefore, a 15° AOA is deemed a realistic upper limit to evaluate in this optimisation. The lower bound is set to $\alpha = 10^\circ$, as any angle of attack smaller than this is unlikely to produce maximum thrust.

The analysis is limited to AWAs between 10° and 150° . Beyond 150° , the drag starts to dominate the thrust (Zhu et al., 2023b) and a deep-stall drag configuration becomes viable. Given its forward speed, a ship encounters these drag-dominated wind angles less frequently than the lift-dominated ones, making this condition less important to analyse. The lower limit of the wind angle range is set to 10° because the wing sails produce negligible thrust in headwind conditions and would thus be retracted to minimise resistance. The incoming wind speed corresponds to a Reynolds number of 1×10^7 , equivalent to a 15 m/s wind over a wing sail with a 14 m chord, as used in Zhu et al. (2023b). The flow has a low Mach number of 0.04, and is therefore assumed to be incompressible.

2.6. Optimisation process

The optimisation process is illustrated in Fig. 4, and its corresponding algorithm is shown in Algorithm 1. The process begins by generating the initial dataset S_o using simulation software. The best sample in S_o , defined as the one with the highest ψ_o , in this case \overline{C}_t , is selected as ϕ_{best} . This initial dataset is then used to train the Gaussian Process surrogate model \mathcal{GP}_0 . Both \mathcal{GP}_0 and ϕ_{best} are passed to the *minimize* function from Scipy. To maximise UCB(ϕ), the function is set to minimise $a(\phi) = -\text{UCB}(\phi_*)$, using the SLSQP algorithm (Virtanen et al., 2020; Kraft, 1988). The *minimize* function returns the minimised sample ϕ_{next} . The simulation software is then used to evaluate ψ_{next} . If ψ_{next} is greater than ψ_{best} , then ϕ_{next} becomes the new ϕ_{best} . Otherwise, ϕ_{best} remains unchanged. In either case, the pair $(\phi_{next}, \psi_{next})$ is added to the dataset to refine the surrogate model. In the next iteration, ϕ_{best} is input to the *minimize* function. This process is repeated for a fixed number of 100 iterations.

Algorithm 1: Bayesian optimisation using minimize.

```
Input: Initial dataset S_o(\phi_o, \psi_o), number of iterations T,
                constraints C
     Output: Best found point \phi_{best}
 1 Train Gaussian Process surrogate model \mathcal{GP}_0 on S_o
 2 Set \phi_{best} \leftarrow \arg \max_{\phi_o \in S_o} \psi_o
 3 for t \leftarrow 1 to T do
           Set \phi_0 \leftarrow \phi_{best}
 4
           Define acquisition function a(\phi_*) = -UCB(\phi_*)
 5
           \pmb{\phi}_{\textit{next}} \leftarrow \mathsf{minimize}(\textit{a}(\pmb{\phi}), \pmb{\phi}_0, \mathcal{GP}_0, \mathcal{C})
 6
           \psi_{next} \leftarrow \text{Simulation software}(\phi_{next})
 7
           if \psi_{next} > \psi(\phi_{best}) then
 8
                 \phi_{best} \leftarrow \phi_{next}
 9
10
11
           Add (\phi_{next}, \psi_{next}) to dataset
           Retrain Gaussian Process on updated dataset
13 end
14 return \phi_{best}
```

2.7. CFD Method - IDDES

To validate the optimisation results, both the optimised aerofoil and the D2R10 reference aerofoil (Zhu et al., 2023b) are analysed in

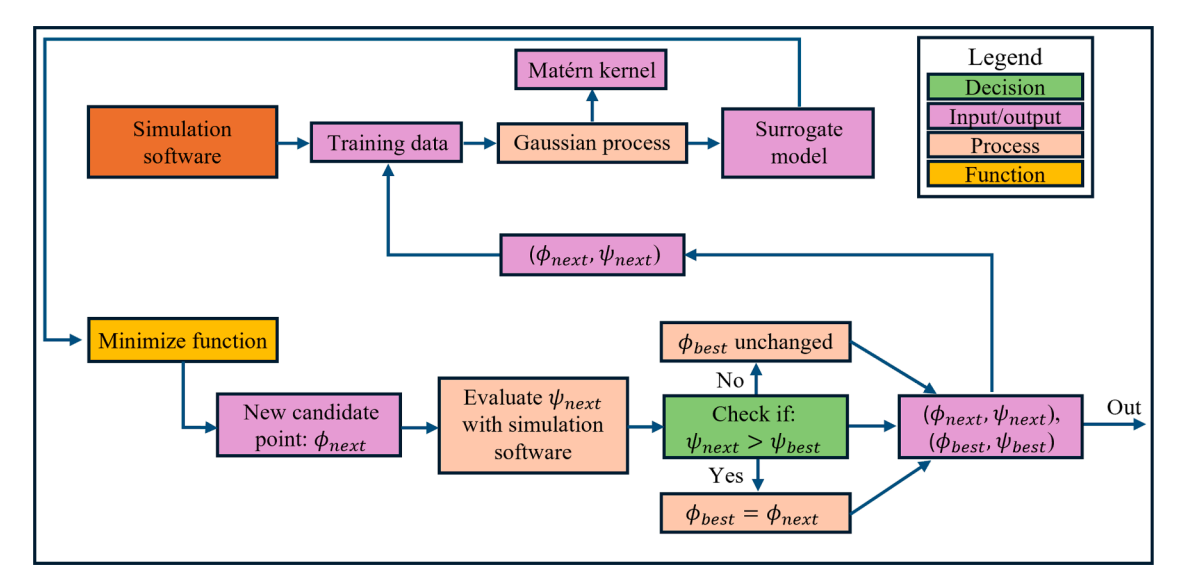


Fig. 4. The flowchart of the optimisation process.

three dimensions using Improved Delayed Detached Eddy Simulation (IDDES) in STAR-CCM+, and the $k-\omega$ SST turbulence model is used. The simulation setup closely follows the methodology described by Zhu et al. (2024, 2023a), where the current setup has been validated. The Reynolds number is 1×10^7 . In the present simulations with a time step of 5×10^{-5} , the fully developed flow fields were obtained after 100 periods of the flow passing through the aerofoil, where the period is calculated based on the freestream flow speed and chord length. After the flow fields were developed, the time-averaged values were calculated based on the data over 150 periods.

The 3D wing sail model is generated by scaling the aerofoils to a chord length of 14 m and extruding them vertically to a height of 72 m along the z-axis. The simulation domain, illustrated in Fig. 5, is a rectangular box measuring 600 m in length, 300 m in width, and 360 m in height. A velocity inlet boundary condition is applied to the front face of the domain, while a symmetry boundary condition is imposed on the bottom face. The remaining faces are assigned pressure outlet boundary conditions. A no-slip wall condition is applied to the surface of the wing sail, and its bottom end is fixed to the domain's lower boundary.

An unstructured mesh consisting of approximately 21 million cells is employed for the simulation. To accurately resolve the boundary layer, 65 prism layers are applied along the geometry walls, with a total thickness of 0.5 m. The setup results in y+ values around 1.0 near the wall. Contours of y+ are illustrated for the BN4 and D2R10 at 15° in Fig. 6, which are visualized with a logarithmic scale. As can be seen, the majority of the wing sail surface shows small values lower than 1.0. The maximum value is 1.6 and 1.9 for the BN4 and D2R10, respectively, but the areas above 1.0 are very small and barely visible.

The mesh is refined near critical regions, such as the leading and trailing edges, with cell sizes around 0.08 m. Fig. 7 presents an overview of the near-field mesh, along with a close-up view of the mesh refinement at the leading edge, for the D2R10 and the optimised aerofoil obtained with the present ML framework (see the discussion in the next section of results and analysis).

3. Results and analysis

3.1. NeuralFoil validation of D2R10

In order to validate the predictions by NeuralFoil, the solver was used to estimate C_l and C_d across AOA ranging from 0° to 20° for the

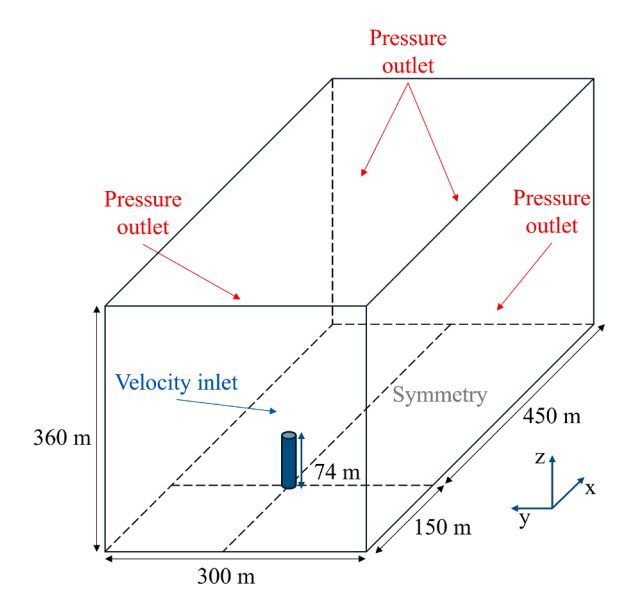


Fig. 5. Schematic of the CFD domain, including the dimensions and boundary conditions. Note that the cylinder is representative of the wing sail.

D2R10. These predictions were then compared with the 3D unsteady RANS results reported by Zhu et al. (2023b), as shown in Fig. 8. Above 10° , NeuralFoil's predictions for C_l closely match those from the 3D unsteady RANS simulations, suggesting that NeuralFoil is capable of capturing three-dimensional flow effects.

The discrepancy in drag prediction is notably larger, with the CFD results indicating drag values up to 2.3 times higher than those predicted by NeuralFoil. The large discrepancies in the drag prediction are attributed to several reasons. The boundary layer approximation used in XFOIL can underestimate skin friction drag and flow separation. The tool is also limited to 2D without spanwise flow effects, as well as the assumption of steady flow. However, given the drag magnitudes are significantly smaller than the lift magnitudes, the inaccurate drag prediction has a negligible contribution to the calculated \overline{C}_t . NeuralFoil estimates a value of 1.30 for the D2R10, and even when drag is doubled, the value increases only slightly to 1.31, indicating that drag has a minimal influence on this metric.

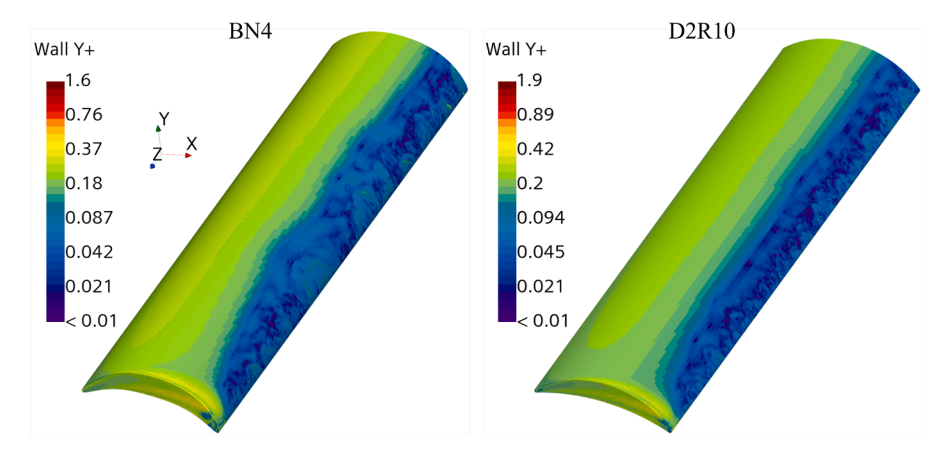


Fig. 6. Contours of y + near the walls of the BN4 and D2R10, visualized with a logarithmic color scale.

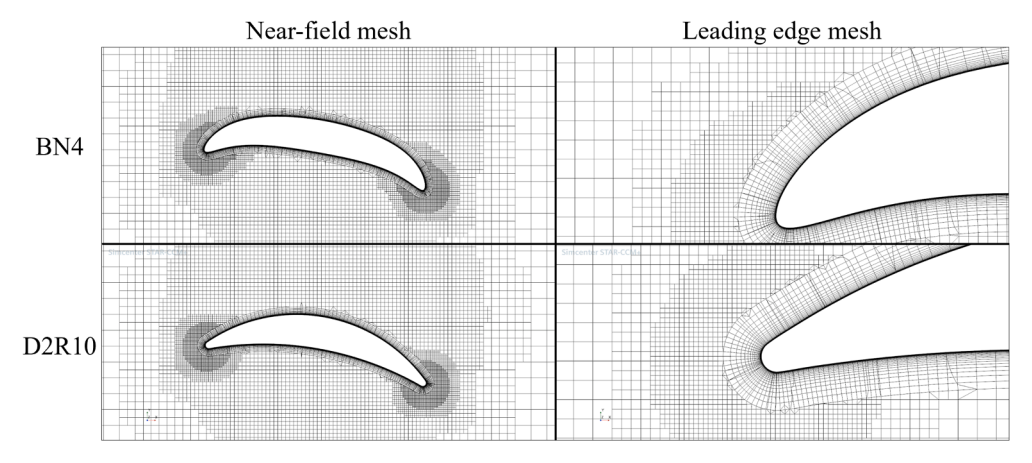


Fig. 7. Cut-plane views of the meshes for the BN4 (the optimised foil using the present method) and the D2R10 (Zhu et al., 2023b) in the near field and around the leading edge at $\alpha = 10^{\circ}$.

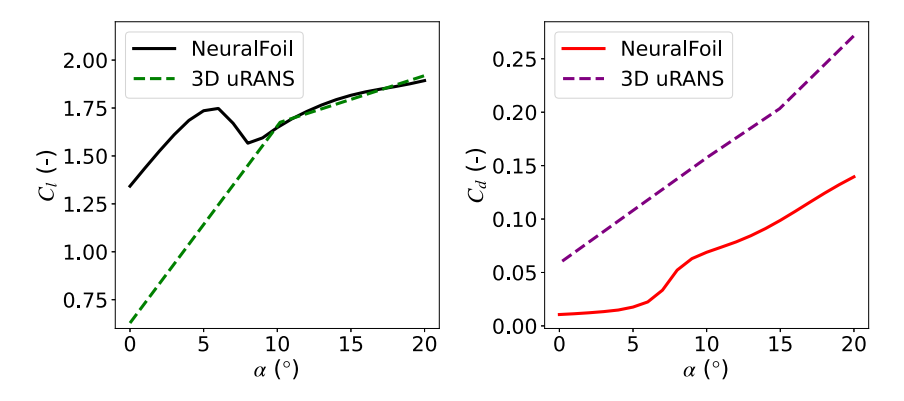


Fig. 8. The lift coefficient (left) and the drag coefficient (right) as a function of AOA from present NeuralFoil and previous 3D unsteady RANS (Zhu et al., 2023b).

3.2. Optimal geometry

Fig. 9 plots both the current and best candidate at each iteration as a green solid line and a red dashed line, respectively. The first point, at iteration zero, is the best sample from the initial design space, referred to as the Initial Aerofoil, with a \overline{C}_t of 1.58. Then, in the first iteration, the optimiser finds a sample with a significantly greater \overline{C}_t of 1.64. The optimiser spends the first 17 iterations exploring the design space be-

fore settling down on an optimum. While exploring the design space, the objective value does not deviate significantly, indicating that the algorithm is more focused on exploitation than exploration.

The new aerofoil resulting from the optimisation is shown in Fig. 10, alongside the Initial Aerofoil and the D2R10. The feature values for the former two aerofoils are presented in Table 2. The most significant change from the D2R10 to the two newly developed aerofoils is the increased thickness away from the centre of the chord. In fact, y_2

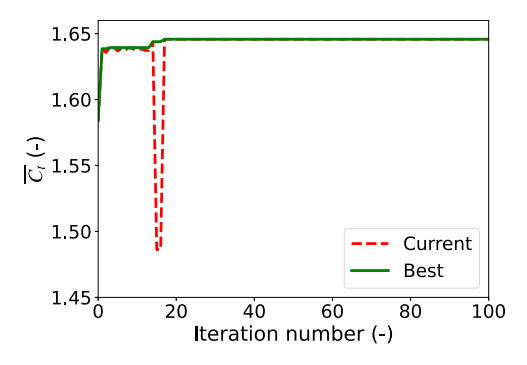


Fig. 9. Predicted thrust results for each candidate aerofoil over 100 iterations (dashed), along with the best candidate identified so far at each iteration (solid).

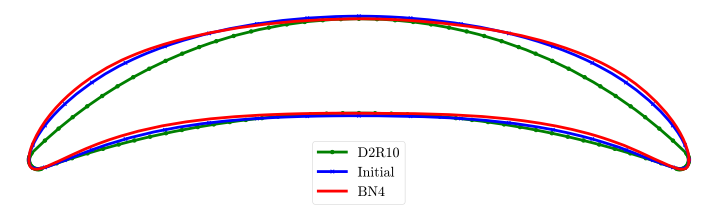


Fig. 10. The three foil profiles such as D2R10 (Zhu et al., 2023b), Initial Aerofoil, optimised BN4.

Table 2Geometrical parameters for the crescent foils.

	I	h_t	x_2	y_2	x_3	<i>y</i> ₃
Initial Aerofoil	7.59	15.21	20.36	12.4	34	9
BN4	8.0	14.29	17.00	12.9	43	8

for the optimised aerofoil is very close to its upper limit. Furthermore, the edge has become more blunt. The difference between the optimised aerofoil and the Initial Aerofoil is less pronounced. Like the D2R10, the optimised aerofoil has the minimum allowable value for h_t , whereas the Initial Aerofoil is comparatively thicker. The latter also exhibits a marginally smaller radius of curvature in the arch. Additionally, the optimised aerofoil has a larger y_2 value than the Initial Aerofoil. The predicted value for \overline{C}_t is 1.65, representing a 4% and 26% improvement over the Initial Aerofoil and D2R10, respectively, while maintaining the same camber. The newly optimised aerofoil will hereafter be referred to as the BN4.

3.3. Sensitivity

Fig. 11 illustrates the sensitivity of \overline{C}_t to various input features based on a sample of 1000 data points. The analysis shows that x_2 and x_3 have minimal influence on \overline{C}_t . In contrast, I exhibits a slight positive correlation, while h_t shows a slight negative correlation, which aligns with the performance difference between the Initial Aerofoil and the BN4. Among all variables, y_2 has the most significant impact, with \overline{C}_t increasing notably as y_2 increases. This finding is consistent with the previously discussed increase in thickness away from the chord centre, as reflected by the higher y_2 value in the BN4. It may also explain why the D2R10 achieves a lower \overline{C}_t than the Initial Aerofoil, despite being thinner.

Lastly, y_3 does not show a clear trend in terms of increasing or decreasing \overline{C}_t , but instead appears to reduce the variability of its possible values as y_3 increases. The reason for this reduction of variability is the curvature constraints, since a higher y_3 moves CP3 upwards relative to CP2, leading to an invalid S-shaped curve. This results in fewer possible valid combinations and, thus, a clustering of the resulting \overline{C}_t .

3.4. NeuralFoil results

The C_l and C_d for all three aerofoils are plotted against α in Fig. 12. The BN4 consistently exhibits the highest C_l , followed closely by the Initial Aerofoil, with the D2R10 trailing behind. In contrast, the D2R10 shows the highest C_d , while the Initial Aerofoil and BN4 alternate. Up to the AOA of $\alpha=13^\circ$, the BN4 experiences higher drag than the Initial Aerofoil. Beyond this point, the trend reverses. This behaviour may be attributed to inaccuracies in drag prediction by NeuralFoil.

The distribution of the thrust coefficient, C_t , over the AWA, θ_{AW} , is presented in Fig. 13. The figure confirms that the BN4 not only has the greatest average thrust but also has superior thrust over all θ_{AW} . The thrust distribution for the Initial Aerofoil is slightly smaller, while the one for the D2R10 is significantly smaller. The results confirm that, within the AWA range from 10° to 150° , a higher lift production leads to higher thrust.

The difference in thrust is most pronounced in the middle of the AWA range, approximately for θ_{AW} between 50° and 110° , and diminishes toward both ends of the range. This AWA range encompasses the crosswind region, where wing sails can produce a large amount of thrust through lift. This is where the BN4 and Initial Aerofoil can outshine the D2R10 with their larger lift production. Outside this range, the influence of the lift relative to the drag decreases. Since the absolute difference in drag between the aerofoils is relatively small, it makes sense that the difference in thrust production becomes less pronounced.

3.5. Flow comparison between BN4 and D2R10 using high-fidelity CFD

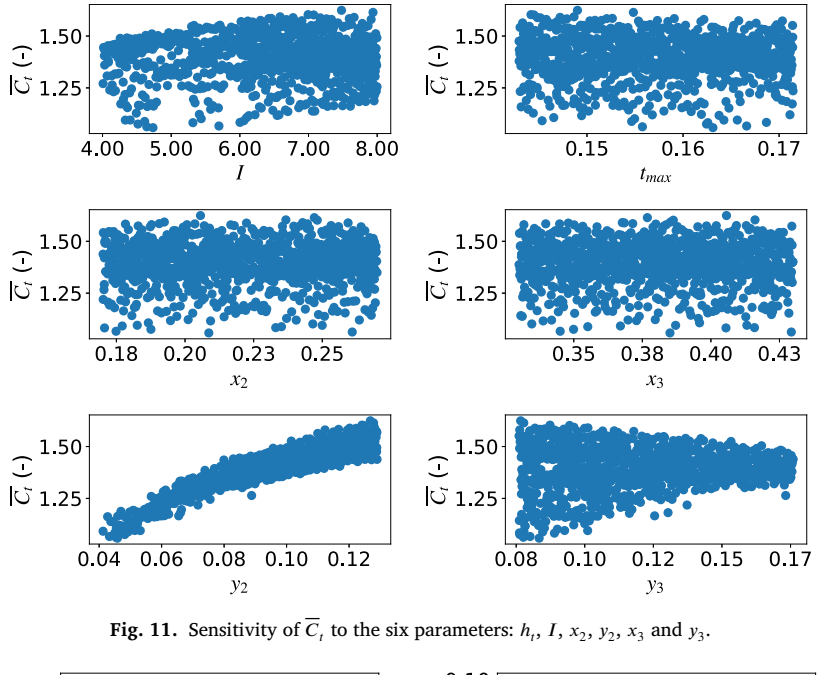
Table 3 presents C_l and C_d for the BN4 and D2R10 aerofoils, as predicted by NeuralFoil and IDDES at $\alpha = 10^{\circ}$ and $\alpha = 15^{\circ}$. The data indicate that NeuralFoil tends to over-predict C_l for the BN4 and underpredict it for the D2R10 while consistently under-predicting C_d for both aerofoils. In order to calculate \overline{C}_t , a linear interpolation of C_l and C_d with respect to the AOA is applied to estimate the intermediate values of C_t . As illustrated by the NeuralFoil trends in Fig. 12, this linearity assumption aligns more closely with the behaviour of C_l than C_d . Nevertheless, as previously shown, variations in C_d have limited influence on \overline{C}_t . While NeuralFoil indicates a 26% performance advantage for the BN4 over D2R10, the CFD-based estimate suggests a more conservative yet still meaningful improvement of 8 %, underscoring a difference in magnitude but not in trend. The discrepancy in thrust prediction between CFD and NeuralFoil can be attributed to the difference in lift prediction. It is also worth noting that NeuralFoil predicts significantly higher lift-to-drag ratios for the BN4 compared to the IDDES results and notably higher ratios than those of the D2R10. However, the IDDES simulations indicate that both aerofoils have similar lift-to-drag ratios in 3D CFD. This suggests that the lift-to-drag ratio may not reliably indicate wing sail performance in these CFD contexts.

Fig. 14 shows streamline and velocity contours for the optimised and reference wing sails at the AOAs of 10° and 15° in the cut-plane aligned with the middle of the span, which are computed from the IDDES. For both wing sails at the specified AOAs, a common phenomenon is that no vortices formed at the leading edges. This is beneficial for the generation of lift force (Zhu et al., 2023b). Meanwhile, the optimised airfoil exhibits a larger high-velocity region near the leading edge, indicating

Table 3The NeuralFoil and IDDES results for the BN4 and D2R10.

		NeuralFoil			CFD				
		C_l	C_d	C_l/C_d	$\overline{\overline{C}}_t$	C_l	C_d	C_l/C_d	\overline{C}_{t}
BN4	10° 15°	2.01 2.27	0.05 0.07	37.67 30.75	1.65	1.80 2.10	0.17 0.22	10.59 9.55	1.50
D2R10	10° 15°	1.65 1.82	0.07 0.10	23.92 18.38	1.30	1.72 1.95	0.15 0.21	11.47 9.29	1.39

Ocean Engineering 342 (2025) 122829



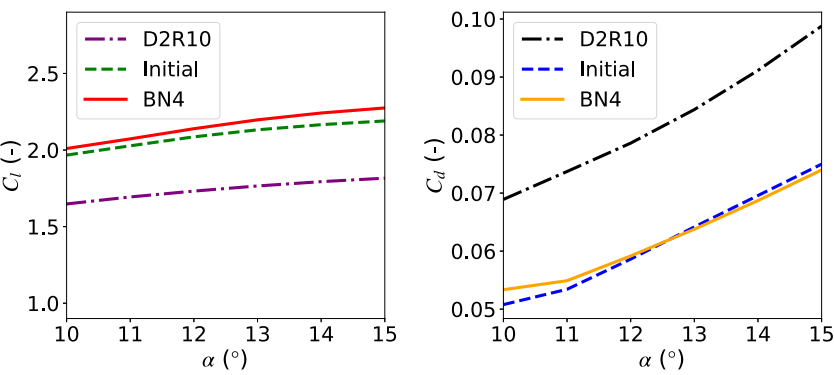


Fig. 12. (left) The lift coefficient and (right) the drag coefficient of the D2R10, the Initial Aerofoil and the optimised BN4, predicted using NeuralFoil.

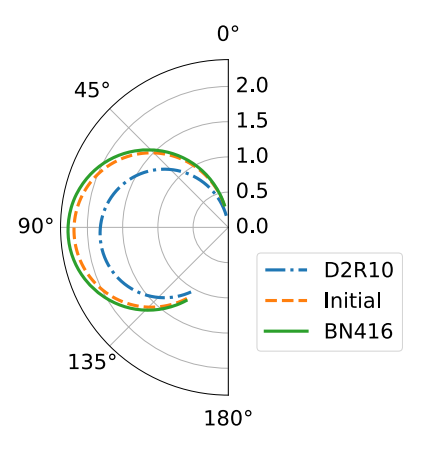


Fig. 13. The distribution of the thrust coefficient, C_t , as function of the AWA, θ_{AW} , for the three different foil profiles.

a lower pressure zone and, thus, greater lift generation. However, flow separation exists on the sucktion side near the trailing edges, which are detrimental to aerodynamic performance with increased drag force but reduced lift force. The optimised wing sail, BN4, delays the onset of the flow separations and consequently induces a smaller recirculation zone in the wake compared to the reference wing sail D2R10. The delayed separation leads to improved aerodynamic performance.

Fig. 15 shows contours of the time-averaged pressure coefficient, \overline{C}_n , on the sail surfaces at the two AOAs. For both of the optimised and reference wing sails, negative $\overline{C_p}$ values are seen over the front twothirds of the suction side from the leading edge. It suggests that most of the lift is generated in this region. In contrast, values in the aft third are much closer to zero, so this part of the surface contributes less to the lift. The sharp change between these regions at the two-thirds location suggests the onset of the flow separation, as also seen in Fig. 14. The sharp changing board shifts forward as the angle of attack increases from 10° to 15° . This means that the flow separation is aggravated when the AOA increases. The low-lift region is more pronounced in the flow of D2R10 than BN4, so its total lift is smaller than the other configuration. Since the lift is the primary contributor to the thrust, the effects result in larger thrust for the optimised configuration BN4. Interestingly, the low $\overline{C_n}$ region does not span the entire wing. At the side edge of the wing, its distribution is changed due to the influence of tip vortices, which is a general aerodynamic mechanism. The tip vortices are responsible for both decelerating and accelerating the flow near the side edge.

The time-averaged skin friction coefficients, $\overline{C_f}$, for the aerofoils at $\alpha=10^\circ$ and $\alpha=15^\circ$ are illustrated in Fig. 16. The contour distribution of this variable is similar to the time-averaged pressure coefficients in Fig. 15, but the regions of large and small magnitudes are oppositely distributed. Because of the flow separation, a sharp board is seen between the regions. Tip vortices at the side edges of the configurations affect the skin friction distribution. It should be noted that the magnitudes of the

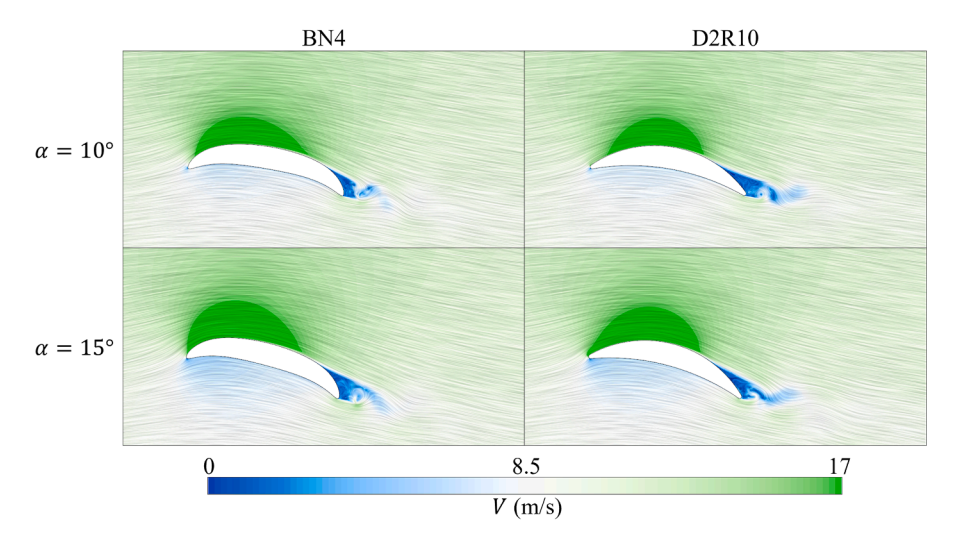


Fig. 14. Streamlines and contours of velocity magnitudes in the cut-plane at the middle span of the wing sails.

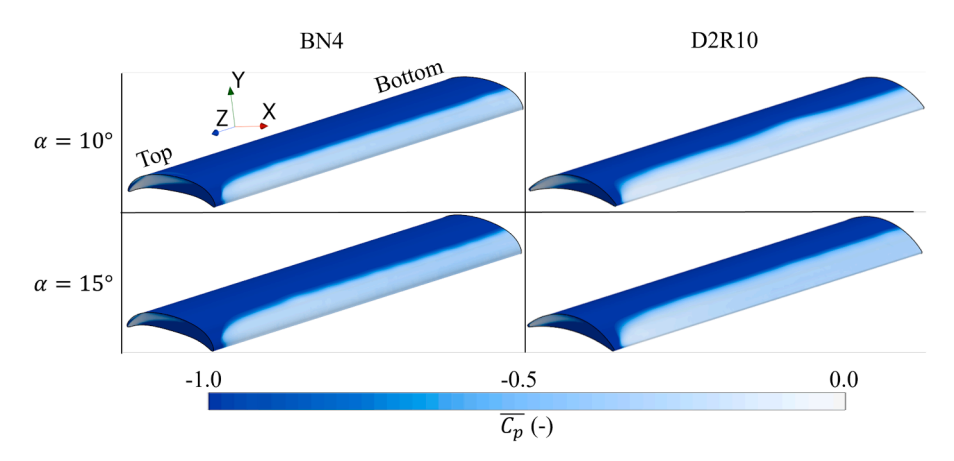


Fig. 15. Contours of the time-averaged pressure coefficient, $\overline{C_p}$, on the surfaces of the BN4 and the D2R10 wing sails at the AOAs of 10° and 15° .

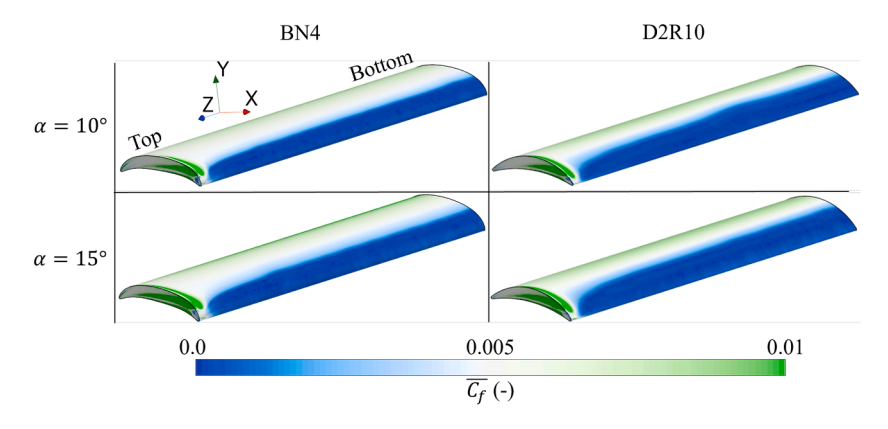


Fig. 16. Contours of the skin friction coefficient, $\overline{C_f}$, on the surfaces for the wing sails, BN4 and D2R10, at the AOAs of 10° and 15° .

skin friction are significantly smaller than those of the pressure. Thus, the contribution of the skin friction in the thrust generation is negligible compared to the pressure differences between the pressure and sucktion sides. This observation is in line with the results in Table 3.

Fig. 17 presents the pressure coefficient, C_p , along the chordwise direction for both AOAs at the spanwise positions of 17.5 m, 35.0 m, and 52.5 m counted from the wing sail root position, which are 25 %, 50 %, and 75 % of the span length, respectively. The varying trends and amplitudes of the coefficient at a specific AOA are nearly the same across the

three spanwise locations. Therefore, the symmetric boundary condition of the computational domain, onto which the wing sail root is mounted, has a limited influence on the pressure distribution. Despite the fact that tip vortices are induced at the side edge, the pressure distributed at 75 % of the span is not affected obviously. This indicates that the aerodynamic performance of the wing sails is dominated by the middle section.

As shown in Fig. 17, on the pressure side, the pressure curves of the two wing sails are similar. And they exhibit a peak value of one at the leading edge, followed by a relatively constant value of approx-

Ocean Engineering 342 (2025) 122829

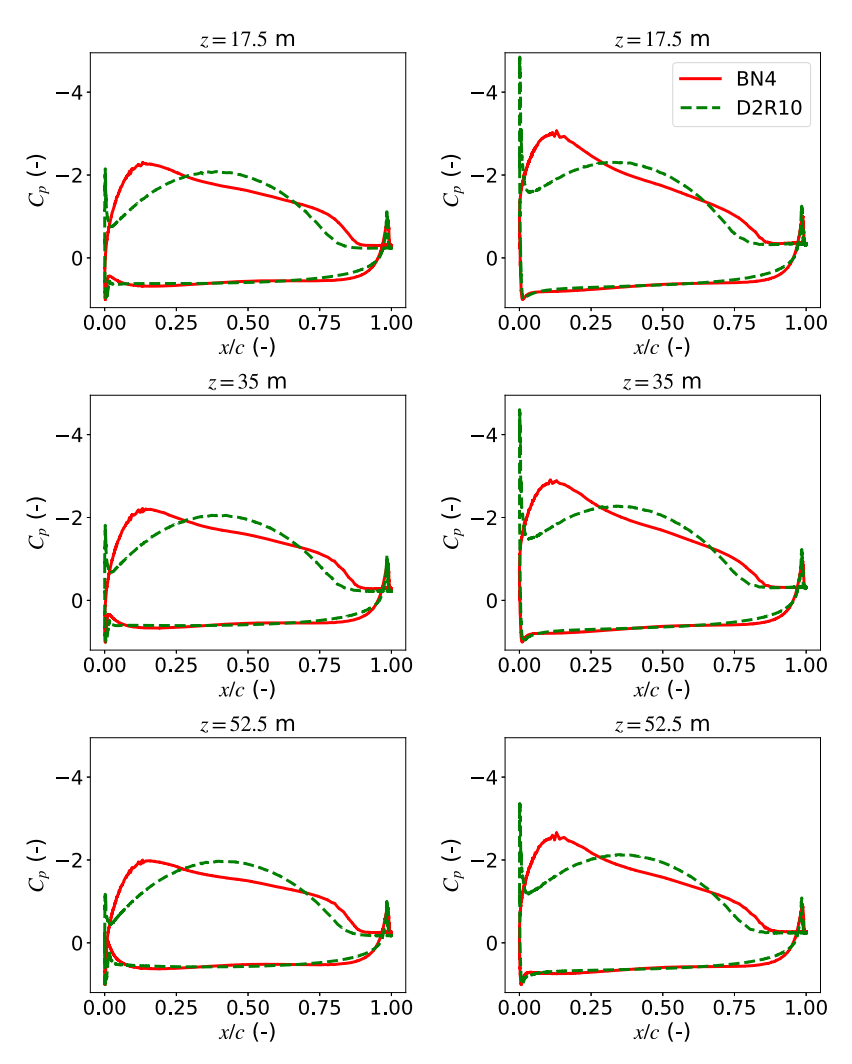


Fig. 17. The distributions of the surface pressure coefficient C_p along the chordwise direction for the AOAs: (left) $\alpha = 10^\circ$ and (right) $\alpha = 15^\circ$. From top to bottom: the spanwise positions are 25 %, 50 % and 75 % of the span length, corresponding to the distances of 17.5 m, 35.0 m, and 52.5 m to the wing sail root.

imately 0.6 along the chord. Beyond the mid-chord, the pressure distributions begin to diverge, with the D2R10 showing a more rapid decrease in C_p . The C_p of the BN4 catches up at the position around 97 % chord. After the position, both sails show a reversing pressure peak, with the D2R10 reaching a slightly lower minimum. This negative pressure peak is attributed to flow separation near the trailing edge, as shown in Fig. 14, which displays streamlines and velocity magnitude contours at the middle of the span. This observation supports earlier conclusions from Figs. 15 and 16. Vortices induced by the flow separation accelerate the local flow on the pressure surface, thereby reducing the local pressure. The pressure distributions on the sucktion side are significantly different between the two wing sails. The D2R10 presents a sharp negative peak at the leading edge, caused by a local velocity increase due to the small tip radius of the configuration, as seen in Fig. 14. The pressure then sharply decreases towards the downstream and reaches the minimum negative values at 40 % and 36 % chord for the AOA of $\alpha = 10^{\circ}$ and $\alpha = 15^{\circ}$, respectively. The BN4 has its smallest pressure at approximately 15% chord for $\alpha = 10^{\circ}$ and 12% chord for $\alpha = 15^{\circ}$. The locations are much closer to the leading edge than those of the D2R10. In the region downstream of the smallest pressure position, the pressure coefficient gradually increases along the chord before rising abruptly due to the flow separation. This abrupt increase occurs earlier for the D2R10. This difference of the flow separation location is also visible in Fig. 14. From Fig. 17, it is clear that the areas enclosed by the pressure coefficient curves of the BN4 are larger than those of the

D2R10. As a result, the BN4 generates larger lift. The figures also indicate that the BN4 achieves its highest lift production closer to the leading edge.

4. Conclusions

In this paper, a machine learning-based optimisation methodology was developed to improve the aerodynamic performance of symmetrically cambered rigid wing sails, which have been considered as one of the concepts with high potential for wind-assisted ship propulsion. Given the special need to maximize the thrust force in multiple large AOAs over a wide range of AWAs, it is impossible to directly adopt conventional optimisation methods that are designated to seek the largest lift force or lift-to-drag in small AOAs. Sampling sectional profiles for wing sails was performed through a novel shape parametrisation approach, in which the camber definition based on Bézier curves is combined with the thickness distribution of modified NACA 4-digit series. The aerodynamics data of the sampled profiles was obtained using NeuralFoil, which is a rapid analysis tool using a neural network trained based on XFOIL. A machine learning-based optimisation approach was developed within a Bayesian optimisation framework. The Gaussian Process was adopted to establish a probabilistic surrogate model that provides both predictions of objective values and estimates of uncertainty. This enables the optimiser to balance exploration and exploitation within the design space.

S. van Reen et al. Ocean Engineering 342 (2025) 122829

The applicability of NeuralFoil for real-world thrust prediction was evaluated by comparing its results to those of the IDDES simulations conducted by Zhu et al. (2023b) for a reference symmetrically cambered aerofoil, called D2R10. The comparison showed that while NeuralFoil provides accurate predictions of lift force, it is inaccurate in drag prediction. This discrepancy is inherited from the method of XFOIL, which produced the training data for the neural network of NeuralFoil. Nevertheless, it was addressed that drag has a minimal effect on the average thrust prediction and, therefore, had little impact on the optimisation outcomes.

The effectiveness of the current optimisation method was demonstrated by analysing the D2R10 aerofoil as a benchmark. The objective was to maximise the average thrust production in the AWA range from 10° to 150° , which represents the most common operation conditions of wing sails encountered in practice. The optimised aerofoil obtained from the current method is referred to as BN4. According to the predictions using NeuralFoil, this optimised design achieved a 26 % increase in the average thrust production. Sensitivity studies revealed that a more uniform thickness distribution along the chord significantly increases the thrust. Moreover, increasing the radii of the leading and trailing edges and reducing the maximum thickness contribute to a modest further improvement.

To confirm the optimised aerodynamic performance, full-size wing sails constructed based on the BN4 and D2R10 under a representative wind speed in the real operation were analysed using the advanced CFD technique of the IDDES. The typical AOAs investigated were 10° and 15°. It was found that the optimal wing sail with the BN4 profile alleviates flow separation, as compared to the benchmark wing sail with the D2R10 profile. Meanwhile, this optimal wing sail induces a larger negative pressure zone formed over the upstream two-thirds of the suction side. And the optimisation leads to a more flattened pressure distribution on the suction side. These effects are essentially beneficial for enhancing the thrust. Compared to XFOIL for NeuralFoil that couples potential flow with boundary layer theory for efficient two-dimensional analysis, IDDES has substantial advantages in modeling turbulence, since it is able to resolve three-dimensional vortices, flow separation, and wake dynamics. According to the present IDDES results, the optimised BN4 increases the thrust by 8%. This value is smaller than the prediction from NeuralFoil, and it is mainly attributed to the overestimation of the lift. Nevertheless, NeuralFoil is effective in making rapid computations while retaining moderate accuracy, which is essential for optimisation involving a large number of samples.

The optimisation methodology in this study employing machine learning techniques in the most computationally intensive steps is demonstrated with the ability to generate aerofoil profiles for rigid wing sails, with meaningful improvements in the average thrust production. Future work is to extend the algorithms to support multi-objective optimisation, allowing for the inclusion of structural characteristics, such as weight. Additionally, high-fidelity simulation methods can be integrated to improve the accuracy of the surrogate model. The framework can be developed to optimise layouts for multi-sail installation.

A limitation of this study is that no experiments were carried out. The reason is that it is challenging to reproduce the flows at the current large Reynolds number of 1.0×10^7 in model-scale wind tunnel tests, because of significant changes in the Mach number and flow compressibility. Nevertheless, future research of great interest is the implementation of full-scale experiments.

CRediT authorship contribution statement

Stephan van Reen: Writing – review & editing, Writing – original draft, Visualization, Validation, Methodology, Investigation, Formal analysis, Data curation; **Berken Serbülent:** Validation, Data curation; **Hua-Dong Yao:** Writing – review & editing, Validation, Supervision, Project administration, Funding acquisition, Conceptualization.

Data availability

No data was used for the research described in the article.

Declaration of competing interest

During the preparation of this work the author(s) used Microsoft Copilot in order to improve the readability and language. After using this tool/service, the author(s) reviewed and edited the content as needed and take(s) full responsibility for the content of the published article.

Acknowledgement

This research was carried out in the project "generic multidisciplinary optimization for sail installation on wind-assisted ships (GEM-INI)" funded by the Swedish Transport Administration. The computations and data handling were enabled by resources provided by the National Academic Infrastructure for Supercomputing in Sweden (NAISS), partially funded by the Swedish Research Council through grant agreement no. 2022-06725.

References

- Blakeley, A.W., Flay, R., Richards, P.J., 2012. Design and optimisation of multi-element wing sails for multihull yachts. In: 18th Australasian Fluid Mechanics Conference, Launcestion, Australia, pp. 3–7.
- Deisenroth, M.P., Rasmussen, C.E., 2011. Pilco: a model-based and data-efficient approach to policy search. In: Proceedings of the International Conference on Machine Learning (ICML)
- Drela, M., 1989. XFOIL: an analysis and design system for low reynolds number airfoils. Conference on Low Reynolds Number Airfoil Aerodynamics, University of Notre Dame. https://doi.org/10.1007/978-3-642-84010-4_1
- Furukawa, H., Blakeley, A.W., Flay, R. G.J., Richards, P.J., 2015. Performance of wing sail with multi element by two-dimensional wind tunnel investigations. J. Fluid Sci. Technol. 10 (2), 15–00256. https://doi.org/10.1299/jfst.2015jfst0019
- Guzelbulut, C., Badalotti, T., Suzuki, K., 2024. Optimization techniques for the design of crescent-shaped hard sails for wind-assisted ship propulsion. Ocean Eng. 312, 119142. https://doi.org/10.1016/j.oceaneng.2024.119142
- Hebbal, A., Brevault, L., Balesdent, M., Talbi, E.-G., Melab, N., 2021. Bayesian optimization using deep gaussian processes with applications to aerospace system design. Optim. Eng. 22 (1), 321–361. https://doi.org/10.1007/s11081-020-09517-8
- Hillenbrand, A., Giovannetti, L.M., Dhomé, U., Kuttenkeuler, J., 2024. Wind tunnel tests of a two-element wingsail with focus on near-stall aerodynamics. J. Sailing Technol. 9 (01), 110–127. https://doi.org/10.5957/jst/2024.9.1.110
- Huang, Z., Yao, H., Lundbladh, A., Davidson, L., 2020a. Low-noise propeller design for quiet electric Aircraft. In: AIAA Aviation 2020 Forum. Online. Session: Emerging Urban Aviation and Electric Aircraft Noise. https://doi.org/10.2514/6.2020-2596
- Huang, Z., Yao, H.-D., Sjögren, O., Lundbladh, A., Davidson, L., 2020b. Aeroacoustic analysis of aerodynamically optimized joined-blade propeller for future electric aircraft at cruise and take-off. Aerosp. Sci. Technol. 107, 106336. https://doi.org/10.1016/j.ast. 2020.106336
- Hussain, M.D., Amin, O.M., 2021. A comprehensive analysis of the stability and powering performances of a hard sail–assisted bulk carrier. J. Mar. Sci. Appl. 20 (3), 426–445. https://doi.org/10.1007/s11804-021-00219-w
- Jacobs, E.N., Ward, K.E., Pinkerton, R.M., 1933. The Characteristics of 78 Related Airfoil Sections From Tests in the Variable-Density Wind Tunnel. Research report 460. National Advisory Committee for Aeronautics.
- Jo, Y., Lee, H., Choi, S., Kwon, J., Ahn, S., 2013. Aerodynamic design optimization of wing-sails. pp. 2013–2524. https://doi.org/10.2514/6.2013-2524
- Khan, L., Macklin, J., Peck, B., Morton, O., Souppez, J.-B., 2021. A review of wind-assisted ship propulsion for sustainable commercial shipping: latest developments and future stakes. Wind Propulsion Conference. https://doi.org/10.3940/rina.win.2021.05
 Kimball, J., 2009. Physics of Sailing. CRC Press.
- Kraft, D., 1988. A software package for sequential quadratic programming. https://www.tib.eu/de/suchen/id/TIBKAT%3A016896521.
- Li, C., Wang, H., Sun, P., 2020. Numerical investigation of a two-element wingsail for ship auxiliary propulsion. J. Mar. Sci. Eng. 8 (5). https://doi.org/10.3390/jmse8050333
- Li, P., Chen, S., 2016. A review on gaussian process latent variable models. CAAI Trans. Intell. Technol. 1 (4), 366–376. https://doi.org/10.1016/j.trit.2016.11.004
- Ma, Y., Bi, H., Hu, M., Zheng, Y., Gan, L., 2019. Hard sail optimization and energy efficiency enhancement for sail-assisted vessel. Ocean Eng. 173, 687–699. https://doi.org/10.1016/j.oceaneng.2019.01.026
- Makram, T.E., Panagiotou, P., Mattheou, D., 2023. Wingsail layout design and shape optimization using a CFD-aided taguchi approach: the aegean marathon case study. Ocean Eng. 276, 114055. https://doi.org/10.1016/j.oceaneng.2023.114055
- Malmek, K., 2023. Rapid Aerodynamic Method for Interacting Sails. Ph.D. thesis. Chalmers University of Technology. Gothenburg, Sweden.
- Malmek, K., Larsson, L., Werner, S., Ringsberg, J.W., Bensow, R., Finnsgård, C., 2024.

 Rapid aerodynamic method for predicting the performance of interacting wing sails.

 Ocean Eng. 293, 116596. https://doi.org/10.1016/j.oceaneng.2023.116596

- Mason, W.H., 2018. Configuration Aerodynamics. Virginia Tech, Blackburg VA.
- Neal, M., Sauze, C., Thomas, B.M., Alves, J.C., 2009. Technologies for autonomous sailing: wings and wind sensors. In: Proceedings of the 2nd International Robotic Sailing Conference (IRSC). Matosinhos, Portugal, pp. 23–30. Presented July 6–12, 2009.
- Nickisch, H., Rasmussen, C., 2008. Approximations for binary gaussian process classification. J. Mach. Learn. Res. 9, 2035–2078.
- Ouchi, K., Shima, K., Kimura, K., 2023. "Wind hunter"- the zero emission cargo ship powered by wind and hydrogen energy. In: Conference Proceedings The Japan Society of Naval Architects and Ocean Engineers 37.
- Ouchi, K., Uzawa, K., Kanai, A., 2011. Huge hard wing sails for the propulsor of next generation sailing vessel. In: Second International Symposium on Marine Propulsors. Hamburg, Germany.
- Ouchi, K., Uzawa, K., Kanai, A., Katori, M., 2016. Wind challenger: The next generation hybrid sailing vessel. In: Smatech Symposium. Glasgow, UK.
- Rasmussen, C.E., 2004. Gaussian Processes in Machine Learning. Springer Berlin Heidelberg, Berlin, Heidelberg. pp. 63–71. https://doi.org/10.1007/978-3-540-28650-9_4
- Rasmussen, C.E., Williams, C. K.I., 2006. Gaussian Processes for Machine Learning. The MIT Press.
- van Reen, S., Zhu, H., Jianfeng, L., Jiqiang, N., Peter, S., Hua-Dong, Y., 2025. Aerodynamic optimization of in-line and parallel layouts for symmetric cambered wingsail installation. Proceedings of the ASME 2025 44th International Conference on Ocean, Offshore and Arctic Engineering (OMAE 2025), OMAE2025–155321.
- Rogers, T.J., Mclean, J., Cross, E.J., Worden, K., 2023. Gaussian Processes. Springer International Publishing, Cham. pp. 121–147. https://doi.org/10.1007/ 978-3.031-36644-4
- Shan, Y., Zhao, S., Peng, F., Yan, R., Tang, X., Su, J., Sun, H., 2025. Sparse representation of robotic machining deformation based on key points determination. In: Lan, X., Mei, X., Jiang, C., Zhao, F., Tian, Z. (Eds.), Intelligent Robotics and Applications. Springer Nature Singapore, Singapore, pp. 3–18. https://doi.org/10.1007/978-981-96-0774-7 1
- Sharpe, P., 2023. NeuralFoil: an airfoil aerodynamics analysis tool using physics-informed machine learning. https://github.com/peterdsharpe/NeuralFoil.
- Sharpe, P., Hansman, R.J., 2025. Neuralfoil: An airfoil aerodynamics analysis tool using physics-informed machine learning. arXiv.https://doi.org/10.48550/arXiv.2503. 16323
- Silva, M.F., Friebe, A., Malheiro, B., Guedes, P., Ferreira, P., Waller, M., 2019. Rigid wing sailboats: a state of the art survey. Ocean Eng. 187, 106150. https://doi.org/10.1016/j.oceaneng.2019.106150
- Snoek, J., Larochelle, H., Adams, R.P., 2012. Practical Bayesian optimization of machine learning algorithms. In: Pereira, F., Burges, C.J., Bottou, L., Weinberger, K.Q. (Eds.), Advances in Neural Information Processing Systems. Curran Associates, Inc.

- Truong, V.K., 2020. An analytical model for airfoil aerodynamic characteristics over the entire 360° angle of attack range. J. Renew. Sustain. Energy 12 (3), 033303. https://doi.org/10.1063/1.5126055
- Virtanen, P., Gommers, R., Oliphant, T.E., Haberland, M., Reddy, T., Cournapeau, D., Burovski, E., Peterson, P., Weckesser, W., Bright, J., van der Walt, S.J., Brett, M., Wilson, J., Millman, K.J., Mayorov, N., Nelson, A. R.J., Jones, E., Kern, R., Larson, E., Carey, C.J., Polat, İ., Feng, Y., Moore, E.W., VanderPlas, J., Laxalde, D., Perktold, J., Cimrman, R., Henriksen, I., Quintero, E.A., Harris, C.R., Archibald, A.M., Ribeiro, A.H., Pedregosa, F., van Mulbregt, P., SciPy 1.0 Contributors, 2020. SciPy 1.0: fundamental algorithms for scientific computing in Python. Nat. Methods 17, 261–272. https://doi.org/10.1038/s41592-019-0686-2
- Wang, X., Jin, Y., Schmitt, S., Olhofer, M., 2023. Recent advances in bayesian optimization. ACM Comput. Surv. 55 (13s). https://doi.org/10.1145/3582078
- Yao, H.D., 2025. Hybrid Parametrization of Symmetrically Cambered (Crescent-Shaped)
 Airfoil Profiles for Rigid Wingsail Design in Wind-Assisted Ship Propulsion. Technical
 Report TR-2025-1. Chalmers University of Technology. Gothenburg, Sweden. https://doi.org/10.63959/m2.techreport/2025.1
- Yao, H.-D., Huang, Z., Davidson, L., Niu, J., Chen, Z.W., 2022. Blade-tip vortex noise mitigation traded-off against aerodynamic design for propellers of future electric aircraft. Aerospace 9 (12), 825. https://doi.org/10.3390/aerospace9120825
- Yasuda, A., Taniguchi, T., Katayama, T., 2024. Numerical investigation of aerodynamic interactions between rigid sails attached to ship. J. Mar. Sci. Eng. 12 (8), 1425. https: //doi.org/10.3390/jmse12081425
- Zhu, H., Chernoray, V., Yao, H.-D., Ringsberg, J.W., Ramne, B., 2023a. Experimental study on structure responses of triple wing sails to turbulence flows at multiple apparent wind angles. In: Advances in the Analysis and Design of Marine Structures. CRC Press, pp. 781–787.
- Zhu, H., Nikmanesh, M.B., Yao, H.-D., Ramne, B., Ringsberg, J., 2022. Propulsive performance of a novel crescent-shaped wind sail analyzed with unsteady RANS in 2D and 3D. Proceedings of the ASME 2022 41st International Conference on Ocean, Offshore and Arctic Engineering (OMAE 2022), Hamburg, Germany, OMAE2022–79867
- Zhu, H., Yao, H.-D., Ringsberg, J.W., 2024. Unsteady RANS and IDDES studies on a telescopic crescent-shaped wingsail. Ships Offshore Struct. 19 (1), 134–147. https: //doi.org/10.1080/17445302.2023.2256601
- Zhu, H., Yao, H.-D., Thies, F., Ringsberg, J., Ramne, B., 2023b. Propulsive performance of a rigid wingsail with crescent-shaped profiles. Ocean Eng. 285 (2), 115349. https://doi.org/10.1016/j.oceaneng.2023.115349